Leveraging graphical models to enhance *in situ* analyte identification *via* multiple voltammetric techniques

Alexis M. Fenton Jr. and Fikile R. Brushett*

Department of Chemical Engineering, Massachusetts Institute of Technology, 77 Massachusetts Avenue, Cambridge, MA 02139, U.S.A.
Email addresses: afenton@mit.edu (Alexis M. Fenton Jr.), brushett@mit.edu (Fikile R. Brushett)
**Corresponding Author: F.R. Brushett*

Abstract

Voltammetry is a powerful analytical technique for evaluating electrochemical reactions and holds particular promise for interrogating electrolyte solutions suitable for energy storage technologies, including examining features such as state-of-charge and state-of-health. However, individual voltammetry techniques are likely to be subcomponents of broader analytical workflows that incorporate complementary methods to diagnose evolving electrolyte solutions of uncertain composition. As such, we demonstrate that jointly evaluating electrolyte solutions with distinct voltammetric modes can enhance the capabilities and sensitivities of characterization protocols. Specifically, by considering macroelectrode cyclic square wave and microelectrode cyclic voltammograms in sequential ("one after another") and simultaneous ("all at once") manners, the composition of an electrolyte solution may be estimated with greater accuracy, and analytes that exhibit near identical electrode potentials may be more readily differentiated. We explore means of further improving this method, finding that protocol accuracy increases when multiple voltammetry techniques are included in the training dataset. We also observe that the algorithm typically becomes more confident—but not necessarily more accurate—when the potential mesh granularity becomes finer. Overall, these studies show that the sequential and simultaneous methods may hold utility when evaluating multiple voltammetry datasets that, in turn, may be leveraged to streamline diagnostic workflows used to examine electrolyte solutions within electrochemical technologies.

Keywords: Cyclic square wave voltammetry, microelectrode voltammetry, analyte identification, Bayesian inference, physics-based modeling, phenothiazine

1. Introduction

Voltammetry is a foundational electroanalytical technique that has been leveraged for more than a century to evaluate electrochemical reactions, ranging from estimating fundamental transport and kinetic rate constants of analytes within well-defined electrolyte solutions to characterizing constituent components within electrolyte solutions of unknown, and sometimes evolving, composition in electrochemical devices.[1–10] Often, physical models—either closed-form or otherwise (e.g., finite difference formulations)—accompany voltammetric experiments to facilitate quantitative interpretation of data collected.[1,10–16] This union of experiment and simulation provides insights into the physical processes that underpin the current response to changes in the electrode potential, leading to the codification of canonical relationships (e.g., Randles-Ševčik equation, Nicholson relation)[17,18] for a variety of potential waveforms, including cyclic linear sweep voltammetry (i.e., "cyclic voltammetry" (CV)), square wave and cyclic square wave (CSW) voltammetry, and alternating-current voltammetry.[10,12,19–24]

The physical size and rotation rate of the disk electrode can be tuned to change the characteristic current response to electrode polarization. Of note, the nature and scaling of voltammograms can be readily altered by modulating the radius of the working electrode by multiple orders of magnitudes (often μm to mm). Larger electrodes, or "macroelectrodes" (radius *ca*. 1 mm), typically engender a linear boundary layer that results in a transient response, while smaller electrodes—"microelectrodes" (radius *ca*. 5 μm)—typically experience a near-hemispherical boundary layer that results in near-steady-state behavior.[2,3,10,13–15,25–30] Despite this versatility, voltammetric methods have certain limitations; as particularly salient examples, they only sense electrochemically-active compounds, and chemical structures cannot be directly discerned. Some of these limitations may be overcome by coupling with other techniques—such

as electrochemical cell cycling (either galvanostatic or potentiostatic), ultraviolet-visible spectrophotometry (UV-Vis), or sufficiently distinct modes of voltammetry (*vide infra*)—to enable more comprehensive analysis.[4,31–34]

A recent direction in the field has focused on integrating voltammetric methods with computational analyses to improve the robustness of established methods and potentially extract greater value from incomplete, convoluted, or otherwise complex data sets (e.g., multicomponent solutions). These methods have been developed for a variety of purposes, including analyte detection (e.g., biomarkers, explosive compounds) and property quantification (estimating transport and electrochemical features).[35–48] However, these computational approaches often leverage physics-agnostic methods (e.g., support-vector machines, partial least squares regression) that are difficult to extrapolate to conditions not directly examined in the training data.[46–49] In this vein, the integration of physical models into computational voltammetry algorithms may build upon the demonstrations already present in the field to enable more powerful algorithms. Efforts towards physics-augmented machine learning algorithms for voltammetry are already underway; indeed, inferential algorithms, combined with a physics-based voltammetry simulator (e.g., MECSim), can estimate parameter values and can even discriminate between candidate electron transfer mechanisms (e.g., Butler-Volmer, Marcus-Hush).[23,24,50,51] Similarly, we ourselves have shown that physical models, binary hypothesis testing, and Bayesian inference can identify dissolved redox-active analytes, which may be useful for advancing *in situ* and *operando* characterization of electrochemical systems.[1] A general summary of this formulation to identify redox-active compounds in electrolyte solutions is shown in **Figure 1**.

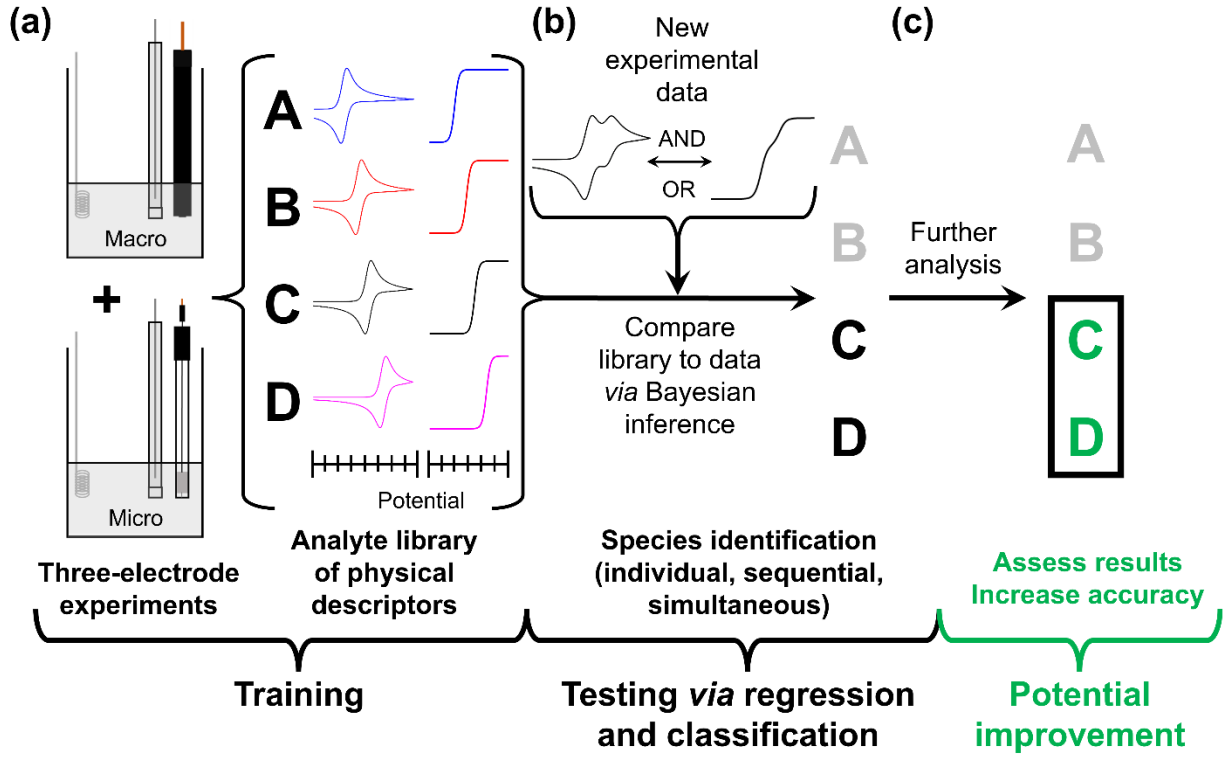

Figure 1. *Flow diagram illustrating how compounds can be identified from multiple voltammetric techniques using Bayesian inference. (a) First, the training process involves experimental three-electrode studies of individual compounds used to assemble a library that catalogues physical descriptors for each species. "Macro" and "Micro" respectively refer to macroelectrode and microelectrode voltammetry, both of which are used in this work; the corresponding potential axes are not to scale. (b) Subsequently, to test the protocol, previously unseen experimental data are subsequently presented, and the catalogued descriptors are used to simulate multiple types of voltammograms. These are then compared to the experimental data using a regression step followed by a classification step that utilizes Bayesian inference to output the probability that each analyte is present in the solution being tested. (c) Finally, additional analyses can also be conducted to assess these results and potentially improve the inferential process.*

In this example system containing four compounds (A–D), the training in **Figure 1a** is conducted by developing a library that contains the physical descriptors (e.g., redox potential, diffusion coefficients) for the oxidized and reduced forms of each compound; these are estimated by evaluating voltammograms of each species in isolation. Once the training is complete (i.e., the library is constructed), the algorithm is tested according to **Figure 1b**. Specifically, previously unseen experimental data are pre-processed (e.g., background signal subtraction) and introduced into the compound identification protocol to label the composition of the electrolyte solution from

which the voltammogram was obtained. Modeled voltammograms normalized by analyte concentration (i.e., output units of A m^3 mol^{-1})—simulated using the physical parameters from the library—are then regressed to the experimental data by adjusting the concentration weights. The presence of each compound is subsequently classified using binary Bayesian hypothesis testing (i.e., it is either present or absent) based on the goodness-of-fit between the modeled and experimental voltammograms. Output probabilities are calculated and reported using Bayes' Rule and Bayes' Information Criterion, and compounds with a probability of 50 % or greater are declared present.

Though not directly pursued in our prior study, data obtained *via* other methods of interrogation (e.g., nuclear magnetic resonance (NMR), mass spectrometry, alternate electrochemical methods), as highlighted by the green text in **Figure 1c**, may be necessary to support—and potentially improve—the outcomes of this protocol. The initial demonstration of this algorithm, where only a single voltammogram was analyzed, was successful across a range of conditions and multiple macroelectrode voltammetric waveforms (CV and CSW voltammetry), but its failure to correctly determine solution compositions at higher CV scan rates (200–1000 mV s^{-1}), along with its inability to differentiate degenerate compounds—those with very similar redox potentials (≤ 15 mV)—emphasizes the need for improved detection accuracy.[1]

Accordingly, we introduce a second analytical technique to improve the overall accuracy of the compound identification protocol. In principle, any non-redundant technique can be implemented, so long as the data quality is sufficient. We specifically explore suitably distinct voltammetry techniques—macroelectrode CSW and microelectrode CV (henceforth referred to as "microelectrode voltammetry")—to explore the feasibility of this approach. More distinct methods of interrogation (e.g., macroelectrode CV and UV-Vis) are hypothesized to jointly extract more

information from a system of interest, as each technique can probe more features of an electrolyte solution that the other methods cannot discern.

In this work, we first discuss how two voltammetry modes can be integrated by using two approaches: sequential ("one after another") and simultaneous ("all at once") analyses. We then examine the performance of the sequential method and compare it to the results from individual analyses of macroelectrode CSW and microelectrode voltammograms. Subsequently, we demonstrate that simultaneous evaluation of CSW and microelectrode voltammograms is particularly sensitive to experimental errors but, when the experimental parameters and library content are sufficiently accurate and precise, may differentiate between nearly-degenerate compounds—a difficult feat to accomplish using only electrochemical methods (especially those insensitive to chemical structure). Finally, we explore additional strategies to further improve the accuracy of this method. Overall, by using the case study of macroelectrode CSW and microelectrode voltammetry, we demonstrate that implementing two voltammetric techniques—and perhaps multiple experimental techniques in general—may aid in analyses of electrolyte solutions for both fundamental and application-based purposes.

2. Methods

2.1. Experimental

All chemicals were used as received, and all experiments were conducted in a glovebox (MBraun Labmaster) filled with argon (Airgas, purity of *ca*. 100 %, catalog number AR UHP300); the glovebox temperature was measured to be 27 °C using a glass thermometer (VWR®, ± 2 °C). Five phenothiazines were tested in this work—10H-phenothiazine (PT), 10-methylphenothiazine (MPT), 10-ethylphenothiazine (EPT), 10-isopropylphenothiazine (iPrPT), and 10-

phenylphenothiazine (PhPT)—which were synthesized and purified as previously described.[1] We note the oxygen concentration in the glovebox was higher than in our prior report (here, ≤ 50 ppm total on average, as compared to an estimated ≤ 10 ppm in the previous study), though this change appears to have a negligible effect on the behavior of the phenothiazines—at least on the timescales of these experiments—as the algorithm performance and outcomes are consistent with the previous study that examines the exact same analytes.[1] All the materials were opened and stored in the glovebox and were directly transferred from their container to a 5 mL volumetric flask with a plastic spatula to ensure the material mass in the solution matched the balance reading (Mettler Toledo, Balance XS64, 61 g capacity with ± 0.1 mg readability). Every solution studied contained between 1–10 mM of either ferrocene (Sigma Aldrich, 98 %, F408) or phenothiazines, along with 0.1 M tetrabutylammonium hexafluorophosphate ($TBAPF_6$, Sigma Aldrich, ≥ 99 %, 86879) in dichloromethane (DCM, ACROS Organics™, 99.9 %, AC610931000 or Sigma-Aldrich®, ≥ 99.9 %, 650463). Ferrocene was used as an internal standard for the reference electrode in a separate solution (also containing 0.1 M $TEAPF_6$ in DCM) at a concentration between 1–10 mM.[52]

The working electrode was a gold disk microelectrode (Bioanalytical Systems, Inc. (BASi), 10 μm dia., MF-2006)—referred to as the "microelectrode"—or a glassy carbon disk macroelectrode (CH Instruments, 3 mm dia., CHI104)—referred to as the "macroelectrode". Both were polished with 0.05 μm alumina powder (Buehler MicroPolish™ Powder, 4010075) in deionized (DI) water (Millipore, 18.2 MΩ cm), rinsed with DI water, and dried using compressed air. Occasionally, the polishing process was first conducted with 0.3 μm alumina powder (Buehler MicroPolish™ II Powder, 406323016) and then repeated using the 0.05 μm alumina powder. Neither lens paper nor sonication was employed in the polishing process. Appropriate care was taken after polishing to ensure the electrode surfaces did not contact any material aside from air (and in the glovebox, Ar)

prior to immersion in the solution of interest. The Ag/Ag^+ electrode was prepared using a non-aqueous reference electrode kit (BASi, MF-2062) filled with 10 mM silver hexafluorophosphate (Sigma-Aldrich®, 98 %, 208361) and 0.5 M tetraethylammonium tetrafluoroborate (Gotion, > 99.9 %) in acetonitrile (Sigma-Aldrich®, ≥ 99.9%, 34851); since all Ag/Ag^+ electrodes were referenced to the ferrocene redox event, the difference in reference fill solution composition is expected to negligibly impact the reported applied potential. The counter electrode was a Pt coil electrode (BASi, 99.95 %, MW-1033). When not in use, the Ag/Ag^+ reference was stored in the glovebox in a fill solution of the same composition as its inner chamber.

Two voltammetry techniques were employed: CV and CSW voltammetry. CV was conducted using both the microelectrode and macroelectrode, while CSW voltammetry was only conducted with the macroelectrode. All microelectrode studies were performed using a CHI630E potentiostat (CH Instruments, Inc.) and processed using the accompanying program "CHI630E Electrochemical Analyzer", and all macroelectrode experiments were performed on a VSP potentiostat (BioLogic) with EC-Lab® software. All data was also processed with Microsoft Excel and MATLAB® R2020a. The potential bounds were –0.3 V and 0.75 V vs. the Ag/Ag^+ reference electrode; the most negative and initial potential (–0.3 V vs. Ag/Ag^+) was set to be approximately 400–500 mV negative of the ferrocene redox potential to minimize possible distortions of the redox events of interest. The initial scan was oxidative—towards more positive potentials—and the turnaround (i.e., the most positive) potential of the voltammetric experiment (0.75 V vs. Ag/Ag^+) was set to be between 200–400 mV positive of the redox potential of the phenothiazine(s) probed. More specifically, the most positive potential was set far enough away from the phenothiazine redox potential as to minimally influence the voltammogram shape[10] but not so far as to access the second electron transfer event of the

phenothiazine to an appreciable extent,[6] to oxidatively decompose the solution, or to alter the electrode surface chemistry.

Microelectrode voltammograms were acquired at a scan rate of 10 mV s^{-1}, with a rest time of 2 s before acquisition, with a potential step size of 1 or 5 mV (between each data point), and with a sensitivity of $1 \cdot 10^{-8}$ or $1 \cdot 10^{-9}$ A V^{-1}. In turn, the CSW voltammetry step height was either 1 or 10 mV, the pulse height was 50 mV, and the pulse duration (per half-period) was 100 ms, resulting in an effective scan rate of 5 or 50 mV s^{-1}, respectively. The potential was held at its initial, most negative (i.e., reductive) value for 2 s before the initial positive (oxidizing) sweep, and the reported current for each potential step was calculated by averaging the raw current over the last 30 % of the step. Macroelectrode cyclic voltammograms were obtained at 10, 25, 50, 100, 200, and 500 mV s^{-1}; all macroelectrode voltammograms were corrected for resistance-driven potential distortions using the BioLogic protocol "*iR* determination with electrochemical impedance spectroscopy" (the "ZIR" protocol). For the "ZIR" protocol, the working electrode potential was set to its open-circuit value; a sinusoidal potential with a 20-mV amplitude and a 100-kHz frequency was applied, a delay of 10 % of the period duration was added before the measurement, and the reported resistance was the average of four independent measurements. The resistance was compensated 85 % by the software during the experiment, with the remaining 15 % manually corrected after the experiment. The solution resistance was not fully compensated (100%) during data acquisition to avoid possible oscillations in the potentiostat.[53]

To calibrate the applied potential to that of the ferrocene redox event and to estimate the microelectrode radius, a separate solution of ferrocene was probed. To enable rapid transfer of the three-electrode configuration between analyte solutions, two separate vials containing only DCM solvent (no analyte or supporting salt) were used to rinse the electrodes. More specifically, after

removing the electrodes from the first solution containing analytes, they were gently dried with Kimwipes (no lens paper was used)—avoiding direct contact with the working electrode surface—and then transferred to a solvent-containing vial. After residing and being intermittently swirled in the solution for 10–20 s, they were again removed, gently dried with Kimwipes, and inserted into the second vial containing only solvent. The rinsing process was repeated, and after being dried with Kimwipes a second time, they were inserted into the second electrolyte solution. Though somewhat laborious, this approach minimizes cross-contamination, as demonstrated in studies of solutions originally containing only solvent, supporting salt, and ferrocene within Supplementary Information **Figure S1**. For each solution, at least six macroelectrode and six microelectrode voltammograms were acquired for statistical rigor, while fewer (at least three) were obtained for ferrocene solutions probed to enable a degree of statistical rigor while minimizing the risk of electrode fouling.[15,54] For most solutions studied, the microelectrode voltammograms were acquired before the macroelectrode voltammograms.

2.2. Library development

Two compound libraries were utilized in this study. The first—referred to as the "previous library", "prior library", or "old library"—was the same as the one used in our prior study,[1] while the second was developed specifically for this study and is referred to as the "new library". Twelve voltammograms were used to construct each compound entry for both libraries—the previous library used only CSW voltammograms, whereas the new library used eight CSW voltammograms and four microelectrode voltammograms. Below, we describe the construction process for the new library.

2.2.1. Modified library construction from both cyclic square wave and microelectrode voltammograms

The new library construction process is more involved than the process to compile the previous library,[1] as microelectrode and macroelectrode voltammetric responses exhibit different dependencies on the same electrochemical and transport descriptors (e.g., redox potential, diffusion coefficient). In particular, the mid-point potential—defined as the average of the two peaks for reversible macroelectrode voltammograms and as the position of the half-max current for microelectrode voltammograms—relates to the redox potential and the ratio of diffusion coefficients with different scalings, respectively shown in **Equations (1)** and **(2)**.[10] Rather than obfuscating analyses, these distinctions enrich library construction; macroelectrode and microelectrode voltammograms may enable more accurate joint estimates of the true diffusion coefficient ratio and redox potential.

$$E_{\text{mid},i}^{\text{CV}} = E_{0,i}^{\text{CV}} - \frac{R_{\text{G}}T}{2F}\ln\left(\frac{D_{O,i}}{D_{R,i}}\right) \quad (1)$$

$$E_{\text{mid},i}^{\text{UME}} = E_{0,i}^{\text{UME}} - \frac{R_{\text{G}}T}{F}\ln\left(\frac{D_{O,i}}{D_{R,i}}\right) \quad (2)$$

In **Equations (1)** and **(2)**, $E_{\text{mid},i}^{\text{UME}}$ (V vs. a reference redox event) represents the mid-point potential for a microelectrode voltammogram ("UME" is short for ultramicroelectrode voltammetry)—with i (–) representing any generic analyte—while $E_{0,i}^{\text{CV/UME}}$ (V vs. a reference redox event) is the respective estimated redox potential of the couple obtained from macroelectrode and microelectrode experiments; the predicted values are not necessarily equal due to the coupling present in **Equations (1)** and **(2)**. R_{G} (8.314 J mol^{-1} K^{-1}) is the universal gas constant, T (K) is the absolute temperature—typically set at 300.15 K in this work based on the measured glovebox temperature— F (96485 C mol^{-1}) is the Faraday constant, and $D_{O,i}$ and $D_{R,i}$

(both $m^2\ s^{-1}$) are the respective diffusion coefficients of the oxidized and reduced forms of species i. $E_{\mathrm{mid},i}^{\mathrm{CV}}$ (V vs. a reference redox event) is the mid-point potential for a macroelectrode voltammogram of species i; "CV" represents cyclic voltammetry, but this relation also holds for macroelectrode CSW voltammetry of a reversible redox couple[12] and is empirically validated for quasireversible couples in **Figure S2**. Though the temperature for this validation is 298.15 K, the generally observed behavior is robust to minor fluctuations in temperature (e.g., glovebox temperatures of 26 °C – 27 °C (299.15 K – 300.15 K)).

Once the experimental voltammograms were acquired, the diffusion coefficient of the reduced species was determined by using the estimated microelectrode radius, microelectrode voltammograms acquired almost immediately after assembling the three-electrode configuration, and steady-state microelectrode models.[55–57] For this regression process, the redox potential was also estimated, and, for simplicity, the ratio of diffusion coefficients was assumed to be 1 (i.e., $D_{R,i} = D_{O,i}$)—the resulting potential estimate is the mid-point potential, rather than the true redox potential. When estimating these parameters from microelectrode voltammograms, only reversible, or diffusion rate-limited, electron transfers were modeled as, to the best of our knowledge, an exact closed-form expression for a quasireversible (kinetic rate-limited) electron transfer has yet to be derived.

Subsequently, macroelectrode CSW voltammograms were analyzed in the same manner as in our previous study.[1] Namely, both reversible and quasireversible electron transfer mechanisms were assessed, and, unlike when microelectrode voltammograms were evaluated, both $D_{R,i}$ and $D_{O,i}$ were allowed to be free parameters. The results from these parameter estimation routines can be jointly evaluated by rearranging **Equations (1)** and **(2)** to estimate the true ratio of diffusion

coefficients (i.e., $D_{O,i}D_{R,i}^{-1}$), and consequently, the estimated true redox potential. Derivation of **Equation (3)** assumes the true redox potentials are equal across voltammetric modes ($E_{0,i}^{\mathrm{CV}} = E_{0,i}^{\mathrm{UME}}$).

$$D_{O,i}D_{R,i}^{-1} \triangleq d_O^{\mathrm{estim,true}} = \exp\left(\frac{2F\left(E_{\mathrm{mid},i}^{\mathrm{CV}} - E_{\mathrm{mid},i}^{\mathrm{UME}}\right)}{R_{\mathrm{G}}T}\right) \quad (3)$$

$d_O^{\mathrm{estim,true}}$ (–) represents the diffusion coefficient ratio, which can then be substituted directly into **Equations (1)** or **(2)** to predict the estimated true redox potential $E_{0,i}^{\mathrm{estim,true}}$ (V vs. a reference redox event).

As a result, the true diffusion coefficient ratio and the true redox potential can be estimated. These parameters, along with the diffusion coefficient of the reduced species (determined from the initial set of microelectrode voltammograms), were subsequently catalogued. The library used to probe microelectrode voltammograms only considered reversible electrochemical kinetics; the macroelectrode library, in turn, also accounted for quasireversible kinetics (if appropriate). Though multiple simplifying assumptions are invoked in this procedure, the goal of constructing a new library is not to perfectly catalog the physical properties of each phenothiazine, but rather to improve the performance of the protocol compared to when only a single technique is used, which we indeed demonstrate to be possible (*vide infra*).

2.3. Compound identification using both cyclic square wave and microelectrode voltammetry

Compound identification was conducted using a similar framework as previously reported and as discussed in the introduction.[1] To summarize, the physical parameters catalogued in the library were used to simulate macroelectrode and microelectrode concentration-normalized

voltammograms (units of A m^3 mol^{-1}) using the same potential waveform as the experimental data of interest. These normalized curves were then fit to experimental data using weighted least-squares regression; binary hypothesis testing was subsequently conducted using Bayesian inference to classify the presence or absence of each member of the library. For instances involving only a single voltammogram, a uniform (i.e., maximal entropy) prior was used.

Our previous framework was extended to incorporate multiple voltammograms into the inferential process. Two approaches—the "sequential" and "simultaneous" approaches, along with the previous "individual" approach—are presented using graphical representations in **Figure 2**. As previously mentioned, a single ("individual") analysis applies Bayes' rule to only one voltammogram to infer the solution composition. In contrast, sequential analyses transfer information from one inferential process to the next by using the output probabilities from the previous state estimation as the priors for the current state estimation. Here, prior probability mass functions for the CSW voltammetry analyses were the output posterior probabilities from the microelectrode analyses and *vice versa*.

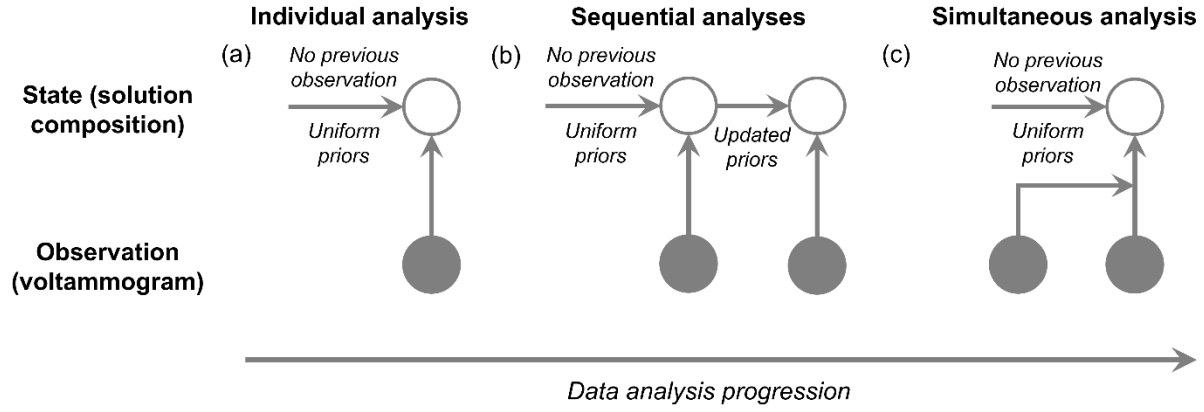

Figure 2. *Graphical models illustrating the inferential workflows utilized in this study. Within each portion, information is processed towards the right. (a) "Individual" analyses: only one observation is evaluated. (b) "Sequential" analyses: two voltammograms / voltammetric techniques are evaluated sequentially. The calculated probabilities from the first dataset serve as the prior probabilities for evaluating the second dataset. (c) "Simultaneous" analyses: two voltammograms / voltammetric techniques are evaluated as one "super-observation", resulting in a single inference.*

2.3.1. Simultaneous analyses

Simultaneous analyses, in turn, utilize the same overall approach of the single inferential processes (i.e., only a single set of probabilities is generated) but increase in complexity, as two voltammograms were concurrently evaluated as a single observation. As such, more detailed treatment is required. The probability distribution function for the simultaneous protocol is treated as a multivariate normal distribution.

$$P_j\left(\boldsymbol{x}_j;\boldsymbol{\mu}_j,\boldsymbol{\Sigma}_j\right)=\det\left(2\pi\boldsymbol{\Sigma}_j\right)^{-\frac{1}{2}}\exp\left(-\frac{1}{2}\left(\boldsymbol{x}_j-\boldsymbol{\mu}_j\right)^{\mathrm{T}}\boldsymbol{\Sigma}_j^{-1}\left(\boldsymbol{x}_j-\boldsymbol{\mu}_j\right)\right) \tag{4}$$

In **Equation (4)**, P_j (–) is the probability distribution function at the j^{th} (–) data point within the string of interest (i.e., the j^{th} point out of N_{t} (–) total points), $\boldsymbol{x}_j$ (units can vary) is the vector-valued random variable of interest at the j^{th} data point, $\boldsymbol{\mu}_j$ (units can vary) represents the vector of average values at the j^{th} data point, and $\boldsymbol{\Sigma}_j$ (units can vary) represents the covariance matrix, also at the j^{th} data point. Note that **Equation (4)** is equivalent to the multivariate normal distribution of the error between the two voltammetric techniques; also note that $\boldsymbol{\Sigma}_j$ is unlikely to be only a diagonal matrix, as both techniques are correlated *via* the physical behavior of the redox-active analyte. Further, as this work only evaluates two voltammetric techniques simultaneously, the dimensions of $\boldsymbol{x}_j$, $\boldsymbol{\mu}_j$, and $\boldsymbol{\Sigma}_j$ are 2 × 1, 2 × 1, and 2 × 2, respectively. In this instance, the covariance matrix can be analytically inverted without significant effort to expand **Equation (4)** and to potentially decrease computation time.

$$P_j\left(\boldsymbol{x}_j;\boldsymbol{\mu}_j,\boldsymbol{\Sigma}_j\right)=\det\left(2\pi\boldsymbol{\Sigma}_j\right)^{-\frac{1}{2}}$$
$$\exp\left(-\frac{\Sigma_j^{1,2}\left(x_{j,2}-\mu_{j,2}\right)\left(x_{j,1}-\mu_{j,1}\right)+\Sigma_j^{2,1}\left(x_{j,1}-\mu_{j,1}\right)\left(x_{j,2}-\mu_{j,2}\right)-\Sigma_j^{2,2}\left(x_{j,1}-\mu_{j,1}\right)^2-\Sigma_j^{1,1}\left(x_{j,2}-\mu_{j,2}\right)^2}{2\det\left(\boldsymbol{\Sigma}_j\right)}\right)$$

(5)

In **Equation (5)**, $x_{j,k}$ (units can vary), $\mu_{j,k}$ (units can vary), and $\Sigma_j^{k,l}$ (units can vary) are respectively the elements of the random vector, average vector, and covariance matrix for the j^{th} data point; k (–) and l (–) are counters. In this work, $\boldsymbol{x}_j$ represents the experimental (difference) current, $\boldsymbol{\mu}_j$ represents the modeled (difference) current, and $\boldsymbol{\Sigma}_j$ represents the approximate experimental covariance.

Within the simultaneous protocol, additional data pre-processing must also be conducted. First, the two voltammograms might not have the same number of points or the same potential scaling—for example, the CSW voltammogram may have a potential mesh granularity of 10 mV while that of the microelectrode voltammogram has a granularity of 1 mV—meaning at least one of the voltammetry data arrays must be resized. In this work, linear interpolation was used to scale the potential mesh of the microelectrode voltammogram to that of the CSW voltammogram. In addition, the potential values may not initially align—for example, after reference electrode potential calibration to the ferrocene redox event, the CSW voltammogram may be measured between –0.5 to 0.55 V vs. $FeCp_2^{0/+}$, while the same of the microelectrode voltammogram may be –0.45 to 0.6 V vs. $FeCp_2^{0/+}$. To avoid issues related to extrapolation arising from these differing potential bounds, data points were manually truncated.

Only one voltammogram for each technique was analyzed, meaning a covariance matrix could not be directly calculated from the experimental data. To resolve this, the covariance matrix was synthetically generated based on the variances for each of the individual techniques. Specifically,

12 random numbers were generated according to a univariate normal distribution for each technique at each data point (i.e., at each applied potential), where the mean was the modeled current and the standard deviations were those predicted from experimental voltammograms of ferrocene. The covariance was calculated between the two strings of 12 random numbers to result in the final covariance matrix. A similar approach was also used to estimate the covariance of the blank electrolyte solution voltammograms—systems containing only solvent and supporting salt—needed for background signal subtraction (see **Figures S9** – **S12**). Though this approach enables individual sets of dissimilar voltammograms to be analyzed, an additional measure of randomness is introduced into the protocol compared to when one voltammogram from a single technique is evaluated. However, based on multiple analyses of the same voltammogram, this added variability does not significantly alter the predicted compositions (e.g., **Table S24**).

2.4. Synthetic data analyses

Synthetic data, generated from the library with added Gaussian noise, was also studied to evaluate the protocol performance in the absence of experimental errors difficult to quantify or to control. Specifically, synthetic data was generated from the new library for both CSW and microelectrode voltammetry. Concentration weights for each compound—and thus the composition of the voltammogram—are set by the user. White (Gaussian) noise was then added with zero-mean and 1 % of the experimental variance for each respective technique, tentatively attributed to potentiostat noise (empirically observed). The remaining 99 % of the standard deviation is attributed to other sources of variability (e.g., glovebox temperature fluctuations, analytical balance imprecision, differing working electrode roughness factors) and can be (and sometimes was) modeled by randomly determining the concentration of each species. However,

including this variability did not appear to impact the protocol accuracy, and at the same time, this approach leaves the user without knowledge of the specified concentration (i.e., ground truth). A visualization of the overall process is presented in **Figure 3**.

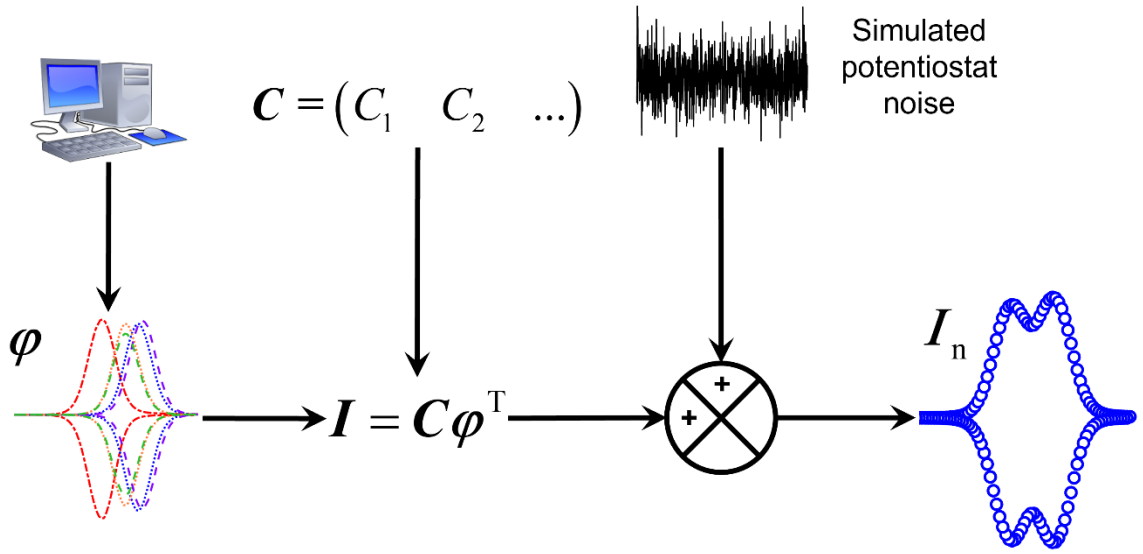

Figure 3. *Visualization of process used to generate noisy synthetic data (in this case, a cyclic square wave voltammogram). First, the physical descriptors from the compound library are used to generate concentration-normalized synthetic voltammograms; the concentration of each species is subsequently specified by the user. Gaussian noise is then added to account for the variability introduced by the potentiostat to result in the final noisy voltammogram.*

In **Figure 3**, $\boldsymbol{\varphi}$ (A m^3 mol^{-1}) is the matrix of concentration normalized currents, $\boldsymbol{C}$ (mol m^{-3}) is a vector of concentrations, C_i (mol m^{-3}) is the concentration of species i, $\boldsymbol{I}$ (A) represents a vector of currents, and $\boldsymbol{I}_{\mathbf{n}}$ (A) represents a vector of noisy synthetic currents. As this synthetic data was directly generated from the existing library and physical (reaction-diffusion) models, data pre-processing was significantly simpler; specifically, no background correction was required, no ohmic losses needed to be compensated, and potential referencing between the Ag/Ag^+ and $FeCp_2^{0/+}$ redox couples was no longer necessary. However, the probability that a signal arose from background noise (e.g., non-faradaic processes)—rather than from the redox event of an analyte—

was still estimated for synthetic data studies to maintain a consistent comparison with experimental analyses. When calculating this probability, the maximum standard deviation of the experimental blank electrolyte solution voltammograms was used instead of analyzing the entirety of the corresponding scan(s).

3. Results and discussion

3.1. Individual analyses

3.1.1. Cyclic square wave voltammetry

Baseline analyses of individual voltammograms can help establish the foundational knowledge needed to assess the performance of the sequential and simultaneous algorithms. As such, CSW voltammograms and microelectrode voltammograms were individually evaluated. The first solution tested was similar in composition to that of our previous study—1 mM PT and 1 mM MPT in an electrolyte solution containing 0.1 M $TBAPF_6$ in DCM—and **Figure 4** illustrates the resulting inferential fitting process for CSW voltammetry.[1]

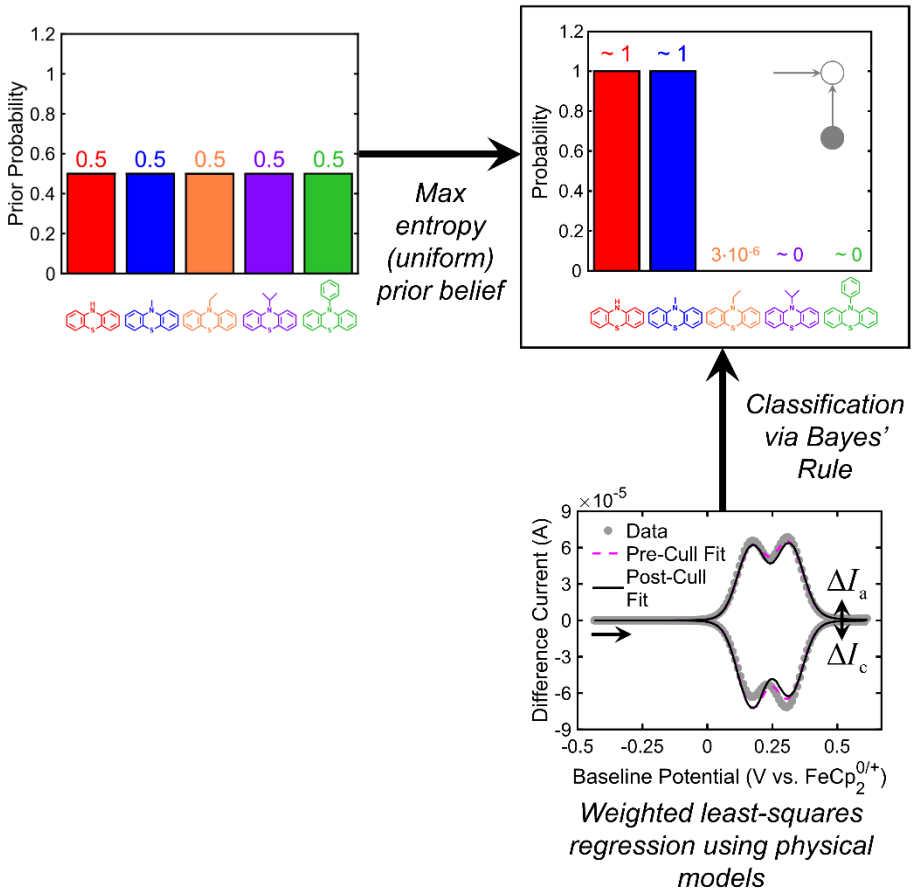

Figure 4. *Analytical workflow for the inferential protocol to identify compounds from a representative CSW voltammogram according to the framework in* ***Figure 2a****, as illustrated by the graphical diagram in the rightmost probability bar graph. The true composition (not revealed to the protocol) is PT and MPT, and the inferred composition is boxed. All probabilities less than* $1 \cdot 10^{-9}$ *are represented as "~ 0". A maximum entropy (i.e., uniform) prior is utilized throughout this work; further, positive difference currents are always oxidative (anodic), negative difference currents are always reductive (cathodic), and the initial potential sweep is always oxidative (see the horizontal arrow).*

In **Figure 4**, the previously unexamined experimental data is introduced on the bottom-right (*via* the CSW voltammogram)— ΔI_a (A) is the anodic (oxidative) difference current, ΔI_c (A) is the cathodic (reductive) analogue, and the horizontal arrow indicates the initial voltammetric sweep is oxidative. Analogous to the process illustrated in **Figure 1**, the physical parameters in the compound library are subsequently used to generate concentration-normalized voltammograms using the same potential waveform as the experimental data of interest. These

normalized voltammograms, in turn, can be linearly regressed to the experimental data *via* least squares by adjusting the concentration weights—this process results in the dashed magenta fit in the same bottom-right graph. This regression is followed by a classification step *via* binary hypothesis testing, where the presence of every individual compound is evaluated by assigning a probability using Bayes' Rule.

In this work, all individual and sequential analyses use a uniform (i.e., maximum entropy) prior when no previous observations are available, as visualized in the top-left bar graph of **Figure 4**. The uniform prior is with respect to the presence or absence of each individual compound, rather than a uniform probability mass function across all five species (where each value would be 0.2). This prior belief is subsequently evaluated with the likelihood function—approximated using Bayes' Information Criterion—and is normalized to output the posterior probability reported in the top-right bar graph, which is subsequently multiplied by the probability that the peak in question is not a background (i.e., non-faradaic) process. Compounds with final probabilities greater than 50 % are classified as present according to the *Maximum a Posteriori* principle, while species with a probability lower than 50 % are eliminated from consideration.[58] Finally, regression is performed with the analytes that remain after the culling—the final fit is represented as the black line in the bottom-right of **Figure 4**. Consistent with our previous work, the protocol is accurate, correctly determining that PT and MPT are present in the solution.[1]

3.1.2. Microelectrode voltammetry

The exact same electrolyte solution was also probed using microelectrode voltammetry—the analysis for a representative microelectrode voltammogram is presented in **Figure 5**. Though the initial regression fits the data well—as illustrated with the dashed pre-cull fit—the classification step eliminates MPT from consideration (i.e., a false negative), indicating

microelectrode voltammetry may not characterize multicomponent solutions as well as macroelectrode CSW voltammetry. The variation in performance is hypothesized to arise from the difference in the shapes of redox events for CSW and microelectrode voltammetry (peaks vs. sigmoids, respectively), which alter microelectrode voltammetry baseline currents when investigating electrolyte solutions containing multiple analytes.

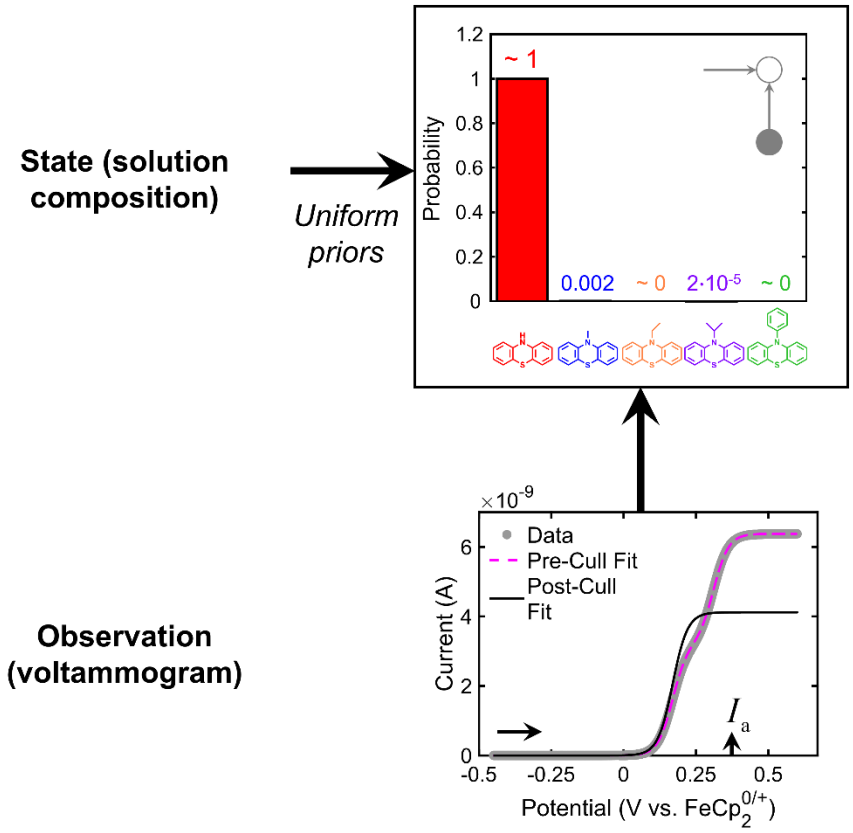

Figure 5. *Evaluation of an individual representative microelectrode voltammogram for composition estimation according to the framework in* ***Figure 2a****, as illustrated by the graphical diagram in the probability bar graph;* ***Figure 4*** *depicts the analogous case for CSW voltammetry. The true composition (not revealed to the protocol) is PT and MPT, and the inferred composition is boxed. Note that uniform priors (****Figure 4****) are utilized. Positive currents are always oxidative (anodic); though not shown, negative currents are always reductive (cathodic); and the initial potential sweep is always oxidative (see the horizontal arrow). All probabilities less than* $1 \cdot 10^{-9}$ *are represented as "~ 0". Note that the horizontal lines below the abscissa likely arise from small bars that represent near- (but non-) zero probabilities and do not indicate negative probabilities.*

I_a (A) is the anodic (oxidative) current. The misidentification in **Figure 5** can potentially be circumvented by including additional data points (e.g., by using a finer potential mesh granularity). Indeed, when a synthetic voltammogram is generated with a potential mesh of 50 μV between each data point (instead of 1 mV per point), the probability of existence for MPT increases to nearly 1 (**Table S21**). However, caution should be used when utilizing this approach, as the routine may not necessarily become more accurate (*vide infra*).

3.2. Sequential analyses

Following the individual voltammetric analyses, the sequential framework (**Figure 2b**) was subsequently evaluated to improve identification accuracy for CSW and microelectrode voltammetric workflows. Specifically, the studies illustrated in **Figure 4** and **Figure 5** are combined by setting the prior probabilities for the CSW voltammetry analysis equal to the posterior probabilities from the microelectrode analysis. In **Figure 6**, the sequential analysis workflow can correctly identify that both PT and MPT are present in the experimental voltammogram. In addition, the probability estimates slightly improve (probability of $< 1 \cdot 10^{-9}$ assigned to EPT) compared to when solely CSW voltammetry experiments are examined (EPT probability of *ca*. $3 \cdot 10^{-6}$), demonstrating the simultaneous method may increase the accuracy of high-performing techniques. This result is also corroborated from the sequential analysis of synthetic data (**Table S17** and **Table S22**). As such, these findings indicate that sequential analyses of voltammograms may correctly infer the solution composition, even if one of the techniques is not completely accurate in isolation. The order in which the techniques were evaluated (i.e., whether CSW or microelectrode voltammograms was assessed first) also did

not affect the output probabilities for the PT-MPT system; namely, minimal "probability hysteresis" was exhibited by the system of interest—however, this may not always be the case (*vide infra*).

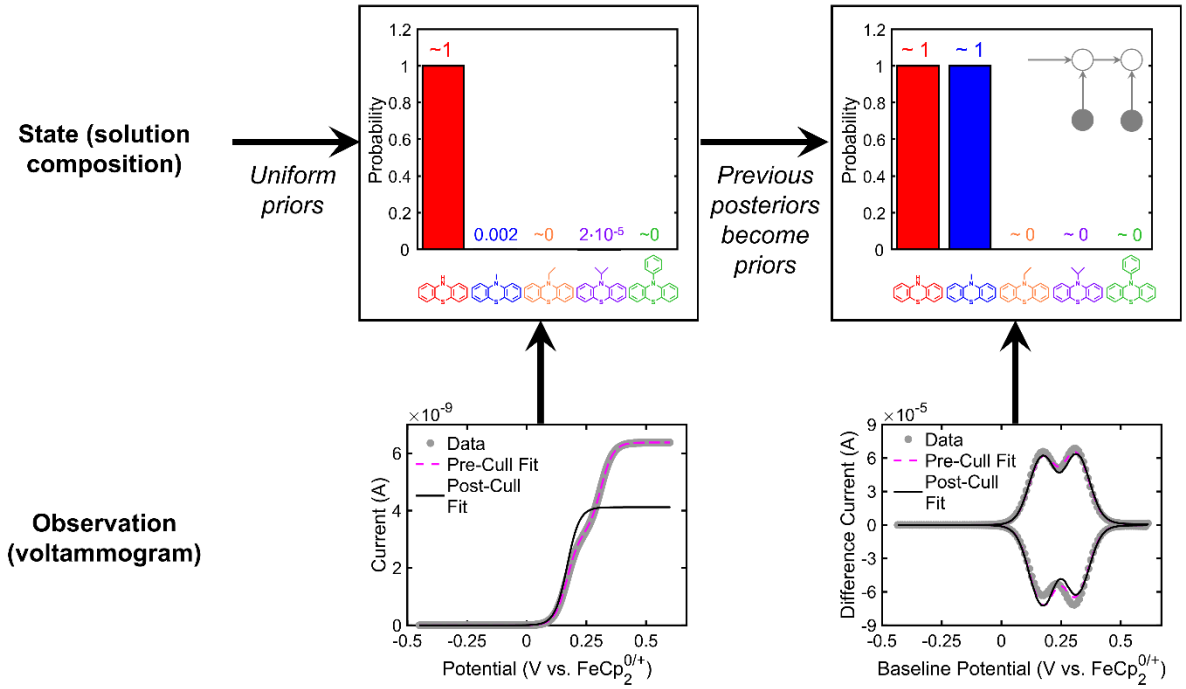

Figure 6. *Sequential evaluation of the same representative voltammograms analyzed in* ***Figure 4*** *and* ***Figure 5*** *according to the framework in* ***Figure 2b****, as illustrated by the gray graphical diagram in the rightmost probability bar graph. Microelectrode voltammetry is evaluated first, followed by cyclic square wave voltammetry. The true composition (not revealed to the protocol) is PT and MPT, and the inferred compositions are boxed. All probabilities less than* $1{\cdot}10^{-9}$ *are represented as "~ 0". Note that the horizontal lines below the abscissa likely arise from small bars that represent near- (but non-) zero probabilities and do not indicate negative probabilities.*

3.3. Simultaneous analyses

The simultaneous approach (**Figure 2c**) was subsequently evaluated; microelectrode and CSW voltammograms are combined as a single larger observation (i.e., a "super-observation"). Beyond potentially improving protocol accuracy as compared to individual analyses, this framework may

differentiate between degenerate compounds. Specifically, the current signal for CSW and microelectrode voltammetry has different power-law dependencies on the diffusion coefficient (approximately 0.5 and exactly 1, respectively), which may enable differentiation between compounds with the same redox potential but dissimilar diffusion coefficients.[10,12]

3.3.1. Simultaneous analysis—PT and MPT blend

Inspired by this distinction in power law dependencies, we first use the simultaneous framework to evaluate the representative CSW and microelectrode voltammograms of the PT-MPT blend studied thus far. Unfortunately, the simultaneous protocol does not successfully classify the solution composition; rather, it predicts that PT, iPrPT, and PhPT are present (two false positives and one false negative). This prediction error is posited to arise from inaccuracies in input parameter estimates—such as the microelectrode radius, which was sometimes observed to differ from its nominal value listed by the manufacturer (perhaps due to sub-optimal in-house polishing)—and in imperfect library construction. This hypothesis is qualitatively supported by the voltammetric fits on the bottom of **Figure 7**—if the concentrations of PT and MPT were increased to better fit the CSW voltammogram data, the simulated microelectrode voltammogram current would also increase, becoming much greater in magnitude than the experimental data. Further, this hypothesis is validated using synthetic data, whose input parameters and library are exactly known; indeed, there, the composition is accurately estimated across seven trials (results in **Table S24**). Additional studies with synthetic data beyond the scope of this work may offer further insight into the performance of the simultaneous protocol (e.g., the sensitivity of the performance of the protocol performance to the estimated microelectrode radius).

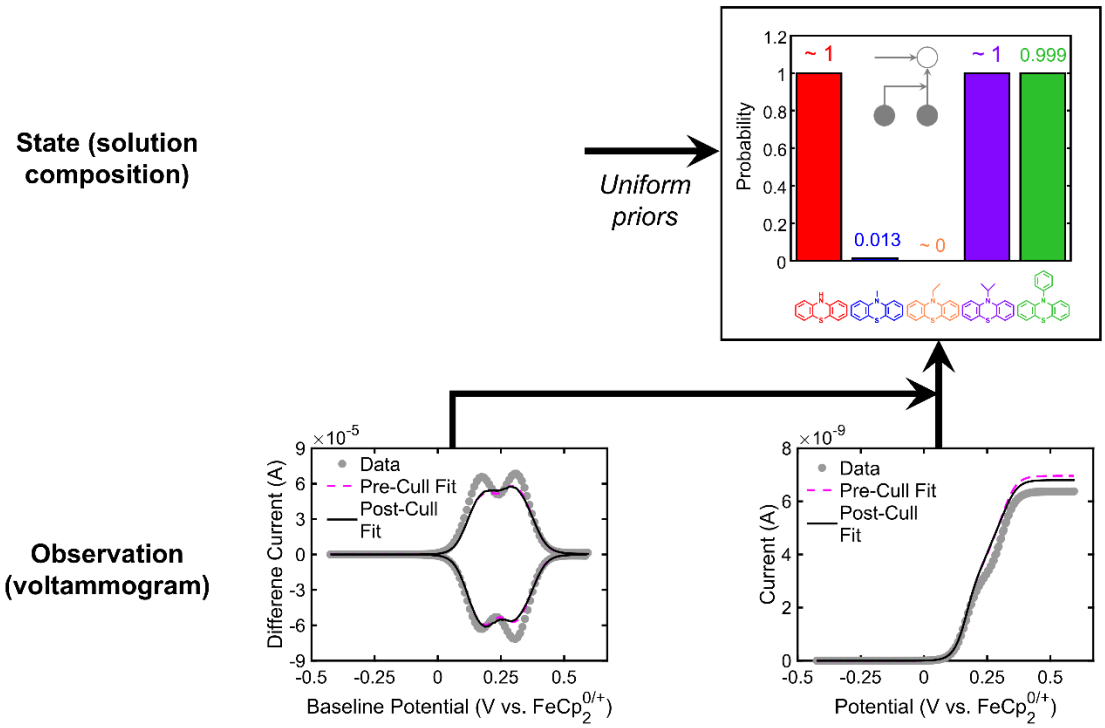

Figure 7. *Simultaneous evaluation of the same representative voltammograms analyzed in* ***Figure 4*** *and* ***Figure 5*** *according to the framework in* ***Figure 2c****, as illustrated by the gray graphical diagram in the probability bar graph. The true composition (not revealed to the protocol) is PT and MPT, and the inferred composition is boxed. All probabilities less than* $1 \cdot 10^{-9}$ *are represented as "~ 0".*

Greater parameter accuracy is necessary because both voltammograms are being regressed using a single set of concentrations. This process contrasts with the individual and sequential analyses—where one set of concentrations is fit per voltammogram—to result in a more restrictive regression process for simultaneous method. As such, we tentatively conclude that the simultaneous analysis, while in principle able to correctly label analytes, suffers in the case of CSW and microelectrode voltammetry because input parameters may be sensitive and require a high degree of accuracy. We also hypothesize this constraint is generally present when using techniques that exhibit physical dependencies on the same parameters, though this currently remains unconfirmed and is beyond the scope of this study.

3.3.2. Simultaneous analysis—EPT and PhPT electrolyte solutions

Despite the practical difficulties that may arise when conducting the simultaneous analysis, the protocol was explored further to determine whether the simultaneous approach could differentiate nearly-degenerate compounds. Specifically, we studied the EPT and PhPT pairing, whose estimated redox potentials differ by *ca.* 1.2 mV. As such, this study may not only help determine the capabilities of the simultaneous approach but also may help reveal general limitations in the protocol when probing nearly-degenerate species.

Three EPT and three PhPT datasets (six total) were studied to evaluate the efficacy of the simultaneous approach with varying degrees of experimental uncertainty. First, synthetic data of both compounds were studied. Subsequently, voltammograms of EPT and PhPT were probed from a solution also studied for library development. By using the same solution, the experimental errors in library construction and the testing data are more likely to be similar, potentially reducing their undesirable effects; moreover, by dividing the voltammograms from this single solution into training and testing datasets, statistically rigorous analyses can be conducted. Finally, experimental voltammograms of EPT and PhPT were analyzed from a different solution than the one used for library construction.

Individual, sequential, and simultaneous analyses for voltammograms of only EPT, taken from one of the solutions used in library construction *via* a training-testing data split, are visualized in **Figure 8**. There, the top right bar plot visualizes four different types of analyses for each compound. For each phenothiazine, the left-most bars (patterned with gray diagonal stripes) depict the estimated composition when only one CSW voltammogram is examined. The left-center bar for each compound (gray dots) depicts the estimated composition when only one microelectrode voltammogram is examined, the right-center bar (gray diamonds) represents the calculated

composition when sequential analyses are studied—minimal probability hysteresis occurs—while the right-most and fully-colored bars indicate the probabilities when the simultaneous approach is conducted. The reported numbers correspond to the estimated probabilities for the simultaneous analysis.

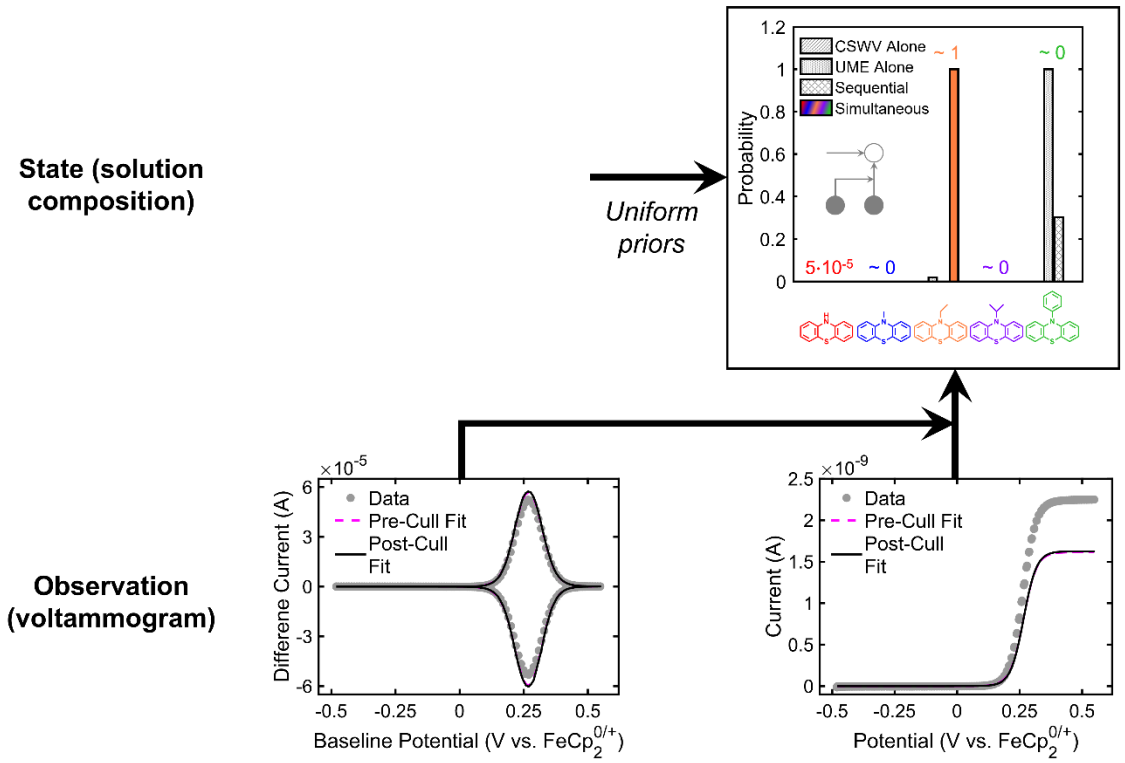

Figure 8. *Analyses of voltammograms taken from a solution examined to catalogue the EPT library entry using a training-testing data split; these specific voltammograms were not used in the construction of the library. In the probability bar graph, the results for the individual and sequential analyses are patterned gray bars, while the results for the simultaneous analysis are shown in full and colored bars. Note that "CSWV" is short for "CSW voltammetry". The reported numerical probabilities are from the simultaneous analysis, as emphasized via the gray graphical diagram from* ***Figure 2c****, and only the observations for the simultaneous analyses are plotted. The true composition (not revealed to the protocol) is EPT, and the inferred composition is boxed. All probabilities less than* $1{\cdot}10^{-9}$ *are represented as "~ 0". Note that the horizontal lines below the abscissa likely arise from small bars that represent near- (but non-) zero probabilities and do not indicate negative probabilities.*

As EPT and PhPT are nearly degenerate, the protocol struggles to correctly identify the solution composition for the individual CSW and microelectrode voltammetry analyses. Unexpectedly, the protocol even estimates that PhPT is present with significant confidence for the

individual microelectrode analysis (probability of 0.9992)—this may potentially be an artifact of imperfect library construction combined with the similar redox potentials of EPT and PhPT (*ca*. 1 mV difference). Sequential analyses also incorrectly classify that no compound is present in the solution, because the only information passed from one observation to the next is the posterior probabilities—the actual voltammograms are not transferred between analyses. Accordingly, within the sequential approach, voltammograms are still individually evaluated during the regression step; the only interaction with other observations occurs during probability computations.

Despite the misidentifications using individual and sequential methods, the simultaneous approach correctly identifies EPT as the only compound present in the solution, demonstrating that this method is potentially capable of differentiating between similar compounds when experimental CSW and microelectrode voltammetry are used as joint techniques. However, the quality of the fits to the experimental voltammograms are not particularly high, suggesting there are likely remaining inaccuracies in the experimental and / or library parameters. This observation is encouraging, as it suggests the parameters do not need to be known with perfect accuracy to identify compounds correctly—rather, they need to meet a particular (presently unquantified) threshold that likely depends on multiple factors, such as the library makeup (e.g., imperfect feature estimations), instrument noise, and solution composition complexity (i.e., the threshold might be more easily met when evaluating single component vs. multicomponent solutions).

Overall, **Figure 8** indicates that the simultaneous method can differentiate nearly-degenerate compounds in an experimental system if the input parameters and the library are known with sufficient accuracy. This analysis also partially reveals further protocol limitations. Specifically, the CSW and microelectrode voltammetry protocols are challenged to identify similar

compounds—such as EPT and PhPT—when testing solutions that were not used for library construction (**Figures S7** and **S8**). This finding also addresses an open query from our prior report; there, fast scan rate CV stymied the ability of the protocol to differentiate between MPT and iPrPT (redox potential difference *ca*. 15 mV), but analogous limitations were not found for CSW voltammetry.[1] Now, an approximate range for the lower bound of the potential resolution can be estimated for CSW voltammetry—between *ca*. 15 mV and *ca*. 1 mV.

3.4. Discussion

Sequential and simultaneous analyses have respective advantages that can improve detection accuracy when CSW and microelectrode voltammetry are used. Sequential analyses can potentially classify systems more accurately than the individual techniques can, even if one of the techniques incorrectly classifies a voltammogram (as is the case with the microelectrode voltammogram of the PT-MPT blend). Though not explicitly studied here, the sequential analysis may also be useful when evaluating time-series data of a transient process (e.g., an electrolyte solution containing decaying redox-active compounds) based on its graphical structure; the previous posterior probabilities serve as an initial guess of the composition at the update time as prior probabilities. In turn, simultaneous analyses of CSW and microelectrode voltammetry are challenged to study electrolyte solutions because multiple input variables, along with the library, must be known with a level of accuracy often difficult to obtain. However, with accurate input parameters—or when the errors in library construction and testing are similar—the method can identify degenerate compounds, as demonstrated with EPT and PhPT, whose estimated redox potentials only differ by *ca.* 1.2 mV.

Despite its promising initial demonstration in this work, the simultaneous method is inherently limited in its ability to differentiate degenerate compounds using voltammetric methods alone; one technique with a unique power-law dependence on the diffusion coefficient is needed for each degenerate analyte. For example, if there were three compounds with nearly the same redox potential (e.g., *N*-propylphenothiazine, EPT, and PhPT),[4] three different voltammetric modes with different dependencies on the diffusion coefficient would be required—for example, rotating disk voltammetry with a proportionality of $D^{2/3}$, microelectrode voltammetry with a dependency on D^{1}, and CSW macroelectrode voltammetry with an approximate scaling of $D^{1/2}$, where D ($m^2\ s^{-1}$) represents a general diffusion coefficient.[10,12] Alternatively, additional spectroscopic techniques (e.g., ^{1}H HMR, UV-Vis) could be implemented to more readily differentiate these specific phenothiazines (or more generally, compounds that present similar electrochemical features). Non-linear unsupervised classification methods beyond the scope of this study may also prove useful in helping to cluster degenerate compounds.[59] Importantly, the fidelity of the library is correlated with the ability of the protocol to distinguish between similar compounds. For example, the library used in the experimental study could accurately label MPT and iPrPT (difference in redox potentials *ca*. 15 mV) but struggled to differentiate EPT and PhPT (difference in redox potentials *ca*. 1 mV). The synthetic data generated from the same library, in turn, labeled EPT and PhPT significantly better—though not perfectly, which is tentatively attributed to the added Gaussian noise and / or to the 10× fewer number of points in the CSW voltammogram that may result in less "confident" estimates (*vide infra*).

As may be expected, the protocol performance improved when multiple techniques are included in the library construction. The library used in this study leveraged both CSW and microelectrode voltammograms; the library from our previous study,[1] which was constructed

exclusively from CSW voltammograms, performed appreciably worse. A comparison of the two libraries is provided in **Table 1**.

***Table 1**: Comparison of the performance of the libraries from our previous work (constructed using CSW voltammograms exclusively)[1] and this work (constructed both from CSW and microelectrode voltammograms) for the experimental voltammograms depicted in **Figure 4** and **Figure 5**. The boxed compositions are the ground truth in all instances. Probabilities less than $1 \cdot 10^{-9}$ are represented as "~ 0".*

Voltammetry Technique	**Probabilities**									
	Library from previous study[1]					**Library from this study**				
	PT	**MPT**	**EPT**	**iPrPT**	**PhPT**	**PT**	**MPT**	**EPT**	**iPrPT**	**PhPT**
CSW (**Figure 4**)	~ 1	~ 1	$3 \cdot 10^{-4}$	~ 0	~ 0	~ 1	~ 1	$3 \cdot 10^{-6}$	~ 0	~ 0
Microelectrode (**Figure 5**)	~ 1	~ 0	~ 0	~ 1	~ 0	~ 1	0.002	~ 0	$2 \cdot 10^{-5}$	~ 0

Table 1 illustrates the superior performance of the library that leveraged microelectrode voltammograms in its construction. Namely, while both libraries resulted in false negatives (no MPT identified for the microelectrode voltammogram in **Figure 5**), only the previous library exhibited a false positive (microelectrode, iPrPT). Interestingly, when sequential analyses are conducted using the previous library, a "probability hysteresis" occurred—when CSW voltammograms were evaluated first, iPrPT is identified in the place of MPT, and vice versa when CSW voltammograms are evaluated second (results in **Table S14** and **Table S15**). This finding suggests that the library must be of a particular quality (presently unquantified) for the sequential analyses of CSW and microelectrode voltammetry to be practically useful. Otherwise, conflicting results (i.e., probability hysteresis) may arise, which may at best confuse the user and at worst misrepresent the solution composition.

It is also important to iterate that a finer potential mesh granularity (i.e., more points per unit volt) does not necessarily mean the protocol becomes more accurate, as mentioned in **Section 3.1.2**. Increasing the number of points typically results in more "confident" predictions, where

probabilities closer to 0 and 1 are respectively assigned for (un)likely compounds. This phenomenon was experimentally examined by acquiring CSW voltammograms with a step height of 1 mV (vs. 10 mV—that is, a finer mesh granularity) of the same PT–MPT blend elsewhere in this work. Microelectrode voltammograms were also acquired with a 5-mV step size between each point, as we were unable to configure the CHI630E potentiostat software (CHI630E Electrochemical Analyzer, last updated in 2021) to have a potential mesh granularity < 1 mV. The results of these analyses when the previous library was used are presented in **Table 2**.

***Table 2**: Comparison of coarser (left-center columns) and finer (right columns) potential mesh granularities using only the library from our previous study (where only CSW voltammograms are evaluated).[1] The CSW voltammogram step height was either 10 mV (211 total points; coarse) and 1 mV (2101 total points; fine), while the potential step was either 5 mV (420 total points; coarse) or 1 mV (2100 total points; fine) for the microelectrode voltammograms. The baseline values used throughout the earlier parts of the study are 10 mV step height for CSW voltammetry and 1 mV step size for microelectrode voltammetry. The boxed compositions are the true compositions in all instances. All probabilities less than $1{\cdot}10^{-9}$ are represented as "~ 0".*

Voltammetry technique	**Probabilities**									
	Coarser potential mesh					**Finer potential mesh**				
	PT	**MPT**	**EPT**	**iPrPT**	**PhPT**	**PT**	**MPT**	**EPT**	**iPrPT**	**PhPT**
CSW	~ 1	~ 1	$4{\cdot}10^{-4}$	~ 0	~ 0	~ 1	~ 1	$2{\cdot}10^{-4}$	~ 0	~ 0
Microelectrode	~ 1	~ 0	~ 0	0.792	~ 0	~ 1	~ 0	~ 0	~ 1	~ 0

As the mesh granularity became finer, the probability increased for compounds that were assigned a non-zero concentration during the regression step, and *vice versa*, with the exception of EPT in the CSW voltammogram. Note that the probability of iPrPT within the microelectrode voltammogram increased as the step size decreased, even though in reality iPrPT is absent. As such, if the potential mesh granularity becomes fine enough, the false positive rate may concurrently increase—namely, a greater number of compounds may be classified as present, when they are actually not present. The converse may also apply—with a coarse enough potential mesh, compounds that are present may be classified as absent (i.e., false negatives), as was the

case for MPT in **Figure 5**; a more detailed analysis of this observation can be found in **Section S7**. As such, users must be cognizant of the number of data points being evaluated; calibrating the potential mesh by assessing the protocol performance on a solution of similar and known composition may enable more accurate identification.

Overall, sequential and simultaneous analyses of CSW and microelectrode voltammetry have the potential to improve detection capabilities, but care must be taken to ensure reliable identification. Specifically, a high-fidelity library must be developed, an appropriate potential mesh must be leveraged, and input parameters (e.g., electrode radius) must be known with sufficient accuracy, especially for simultaneous analyses. When these conditions are adequately met, multiple voltammetric techniques can be integrated to improve the overall performance of the previously-developed compound identification protocol.[1] Compared to the simultaneous workflow, sequential analyses are preferred when evaluating the multiple CSW and microelectrode voltammograms collected in this study. Within this context, simultaneous analyses should be considered only when multiple degenerate compounds are evaluated. The efficacy of these methods should be evaluated when using different techniques or probing new analytes—perhaps by examining a known standard—to validate whether sequential analyses remain the preferred approach.

4. Conclusions

In this work, we explore and expand upon methods to identify redox active compounds from voltammograms using physical models and Bayesian inference. Multiple analytical techniques will ultimately be necessary to identify redox-active analytes confidently and reliably in electrolyte solutions, and as such, we pursue multiple voltammetric methods—here, CSW and microelectrode

voltammetry—which may be readily implemented into electrochemical workflows.[7] Specifically, in the particular case where CSW and microelectrode voltammetry are considered, we demonstrate that sequentially evaluating multiple voltammograms in series improves the overall detection accuracy when a sufficiently accurate library is used. We also show that simultaneous analyses can differentiate between degenerate compounds using these two voltammetric methods, but the input parameters and the library must be more accurate than is necessary for individual or sequential analyses. As such, sequential analyses appear to be the best suited for multicomponent electrolytes studied in this work.

While sequential and simultaneous analyses can accurately classify electrolyte composition, significant work remains to develop a framework capable of probing electrolyte solutions in practical embodiments. For example, sequential analyses are not necessarily guaranteed to perform better for every conceivable technique pairing—the respective capabilities of these workflows, along with the employed techniques themselves, must be judiciously evaluated to determine the most accurate inferential framework for the system of interest. Sequential analyses may also be capable of analyzing time-series data, which could be useful in tracking the evolution (e.g., degradation) of redox-active species. As such, future efforts should be directed towards applying the current compound identification protocol to model evolving systems to further refine its performance.

Additional approaches can be used to differentiate between similar species and generally improve detection accuracy. Information from a broader set of experimental methods—either analytical (e.g., UV-Vis, NMR) or applied (e.g., cell cycling data) in nature—can potentially be incorporated into a similar workflow, so long as these techniques do not provide redundant information and the collected data is of sufficient quality. Alternatively, non-linear and

unsupervised clustering algorithms (e.g., t-distributed stochastic neighbor embedding) can enable classification of degenerate groups;[59] the protocol can then determine the presence of each group of degenerate compounds, rather than the individual species. Though a diversity of approaches and techniques can be integrated in a mix-and-match fashion, the best combination of methods is likely to be domain- and context-dependent.

5. Acknowledgements

This work was supported as part of the National Science Foundation (NSF) under Award Number 1805566. Any opinion, findings, and conclusions or recommendations expressed in this material are those of the author and do not necessarily reflect the views of the NSF. A. M. F. Jr. also gratefully acknowledges financial support provided by the MIT MathWorks Engineering Fellowship. We gratefully acknowledge the MIT Supercloud and Lincoln Laboratory Supercomputing Center for providing HPC resources that have contributed to the research results reported within this paper. We also thank the late Professor Susan Odom, Professor Aman Kaur, and the Odom Research Group for synthesizing, purifying, analyzing, and shipping phenothiazines. We also thank the entire Brushett Research Group for fruitful discussions on data analysis and presentation.

6. CRediT authorship contribution statement

Alexis M. Fenton Jr.: Conceptualization, Methodology, Software, Validation, Formal analysis, Investigation, Data curation, Visualization, Writing – original draft, Writing – review and editing. **Fikile R. Brushett:** Conceptualization, Project administration, Supervision, Writing – original draft, Writing – review and editing, Funding acquisition.

7. Declaration of competing interests

The authors declare that they have no known competing financial interests or personal relationships that could have appeared to influence the work reported in this paper.

8. Glossary

Latin variables

$\boldsymbol{C}$	Vector of concentrations (mol m^{-3})
C_i	Concentration of species i (mol m^{-3})
D	General diffusion coefficient (m^2 s^{-1})
$D_{O,i}$	Diffusion coefficient for the oxidized form of species i (m^2 s^{-1})
$D_{R,i}$	Diffusion coefficient for the reduced form of species i (m^2 s^{-1})
$d_O^{\text{estim,true}}$	Estimated value of the true diffusion coefficient ratio $D_{O,i}D_{R,i}^{-1}$ (–)
$E_{0,i}^{\text{CV/UME}}$	Respective estimated redox potential of the couple obtained from macroelectrode or microelectrode experiments (V vs. reference redox event)
$E_{\text{mid},i}^{\text{CV/UME}}$	Respective mid-point potential for a macroelectrode or microelectrode voltammogram (V vs. reference redox event)
$E_{0,i}^{\text{estim,true}}$	Estimated value of the true redox potential (V vs. reference redox event)
F	Faraday constant (96485 C mol^{-1})
$\boldsymbol{I}$	Vector of currents (A)
I_{a}	Anodic current symbol (A)
$\boldsymbol{I}_{\mathbf{n}}$	Vector of noisy synthetic currents (A)
$\boldsymbol{i}$	Indexing counter (–)
j	Indexing counter (–)
k	Indexing counter (–)
l	Indexing counter (–)
N_{t}	Number of total entries in a dataset (–)
P_j	Probability distribution function at the j^{th} data point of interest (–)
R_{G}	Universal gas constant (8.314 J mol^{-1} K^{-1})
$\boldsymbol{T}$	Absolute temperature (K)
$\boldsymbol{x}_j$	Vector-valued random variable at the j^{th} data point (units can vary)
$x_{j,k}$	k^{th} element of $\boldsymbol{x}_j$ (units can vary)

Greek variables

ΔI_{a}	Anodic difference current symbol (A)
ΔI_{c}	Cathodic difference current symbol (A)
$\boldsymbol{\mu}_j$	Vector of average (mean) values at the j^{th} data point (units can vary)
$\mu_{j,k}$	k^{th} element of $\boldsymbol{\mu}_j$ (units can vary)
$\boldsymbol{\Sigma}_j$	Covariance matrix at the j^{th} data point (units can vary)
$\Sigma_j^{k,l}$	$(k,l)^{\text{th}}$ element of $\boldsymbol{\Sigma}_j$ (units can vary)
$\boldsymbol{\varphi}$	Matrix of concentration normalized currents (A m^3 mol^{-1})

Latin symbols

A	Toy (i.e., example) species
B	Toy (i.e., example) species
C	Toy (i.e., example) species
D	Toy (i.e., example) species
O	Oxidized form of a redox couple
R	Reduced form of a redox couple

9. References

(1) Fenton Jr., A. M.; Brushett, F. R. Using Voltammetry Augmented with Physics-Based Modeling and Bayesian Hypothesis Testing to Identify Analytes in Electrolyte Solutions. *J. Electroanal. Chem.* **2022**, *904*, 115751. https://doi.org/10.1016/j.jelechem.2021.115751.

(2) Bond, A. M. Past, Present and Future Contributions of Microelectrodes to Analytical Studies Employing Voltammetric Detection: A Review. *The Analyst* **1994**, *119* (11), 1–21. https://doi.org/10.1039/AN994190001R.

(3) Stolze, C.; Meurer, J. P.; Hager, M. D.; Schubert, U. S. An Amperometric, Temperature-Independent, and Calibration-Free Method for the Real-Time State-of-Charge Monitoring of Redox Flow Battery Electrolytes. *Chem. Mater.* **2019**, *31* (15), 5363–5369. https://doi.org/10.1021/acs.chemmater.9b02376.

(4) Narayana, K. A.; Casselman, M. D.; Elliott, C. F.; Ergun, S.; Parkin, S. R.; Risko, C.; Odom, S. A. *N*-Substituted Phenothiazine Derivatives: How the Stability of the Neutral and Radical Cation Forms Affects Overcharge Performance in Lithium-Ion Batteries. *ChemPhysChem* **2015**, *16* (6), 1179–1189. https://doi.org/10.1002/cphc.201402674.

(5) Lin, K.; Chen, Q.; Gerhardt, M. R.; Tong, L.; Kim, S. B.; Eisenach, L.; Valle, A. W.; Hardee, D.; Gordon, R. G.; Aziz, M. J.; Marshak, M. P. Alkaline Quinone Flow Battery. *Science* **2015**, *349* (6255), 1529–1532. https://doi.org/10.1126/science.aab3033.

(6) Kowalski, J. A.; Casselman, M. D.; Kaur, A. P.; Milshtein, J. D.; Elliott, C. F.; Modekrutti, S.; Attanayake, N. H.; Zhang, N.; Parkin, S. R.; Risko, C.; Brushett, F. R.; Odom, S. A. A Stable Two-Electron-Donating Phenothiazine for Application in Nonaqueous Redox Flow Batteries. *J. Mater. Chem. A* **2017**, *5*, 24371–24379. https://doi.org/10.1039/C7TA05883G.

(7) Neyhouse, B. J.; Tenny, K. M.; Chiang, Y.-M.; Brushett, F. R. Microelectrode-Based Sensor for Measuring Operando Active Species Concentrations in Redox Flow Cells. *ACS Appl. Energy Mater.* **2021**, *4* (12), 13830–13840. https://doi.org/10.1021/acsaem.1c02580.

(8) Gupta, D.; Cai, C.; Koenig, G. M. Comparative Analysis of Chemical Redox between Redox Shuttles and a Lithium-Ion Cathode Material via Electrochemical Analysis of Redox Shuttle Conversion. *J. Electrochem. Soc.* **2021**, *168* (5), 050546. https://doi.org/10.1149/1945-7111/ac0068.

(9) Voltammetry Retrospective. *Anal. Chem.* **2000**, *72* (9), 346 A-352 A. https://doi.org/10.1021/ac002791t.

(10) Compton, R. G.; Banks, C. E. *Understanding Voltammetry*, 2nd ed.; Imperial College Press: London, 2011.

(11) Compton, R. G.; Laborda, E.; Ward, K. R. *Understanding Voltammetry: Simulation of Electrode Processes*; Imperial College Press: London, 2014.

(12) Bard, A. J.; Faulkner, L. R. *Electrochemical Methods: Fundamentals and Applications*, 2nd ed.; John Wiley & Sons. Inc.: New York, 2001.

(13) Saito, Y. A Theoretical Study on the Diffusion Current at the Stationary Electrodes of Circular and Narrow Band Types. *Rev. Polarogr.* **1968**, *15* (6), 177–187. https://doi.org/10.5189/revpolarography.15.177.

(14) Klymenko, O. V.; Svir, I.; Oleinick, A.; Amatore, C. A Novel Approach to the Simulation of Electrochemical Mechanisms Involving Acute Reaction Fronts at Disk and Band Microelectrodes. *ChemPhysChem* **2012**, *13* (3), 845–859. https://doi.org/10.1002/cphc.201100825.

(15) Kowalski, J. A.; Fenton Jr., A. M.; Neyhouse, B. J.; Brushett, F. R. A Method for Evaluating Soluble Redox Couple Stability Using Microelectrode Voltammetry. *J. Electrochem. Soc.* **2020**, *167* (16), 160513. https://doi.org/10.1149/1945-7111/abb7e9.

(16) Oldham, K. B.; Myland, J. C. Modelling Cyclic Voltammetry without Digital Simulation. *Electrochimica Acta* **2011**, *56*, 10612–10625. https://doi.org/10.1016/j.electacta.2011.05.044.

(17) Elgrishi, N.; Rountree, K. J.; McCarthy, B. D.; Rountree, E. S.; Eisenhart, T. T.; Dempsey, J. L. A Practical Beginner's Guide to Cyclic Voltammetry. *J. Chem. Educ.* **2018**, *95* (2), 197–206. https://doi.org/10.1021/acs.jchemed.7b00361.

(18) Nicholson, R. S. Theory and Application of Cyclic Voltammetry for Measurement of Electrode Reaction Kinetics. *Anal. Chem.* **1965**, *37* (11), 1351–1355. https://doi.org/10.1021/ac60230a016.

(19) Helfrick, J. C.; Bottomley, L. A. Cyclic Square Wave Voltammetry of Single and Consecutive Reversible Electron Transfer Reactions. *Anal. Chem.* **2009**, *81* (21), 9041–9047. https://doi.org/10.1021/ac9016874.

(20) O'Dea, J. J.; Osteryoung, J.; Osteryoung, R. A. Theory of Square Wave Voltammetry for Kinetic Systems. *Anal. Chem.* **1981**, *53*, 695–701. https://doi.org/10.1021/ac00227a028.

(21) Chin, K. Y.; Prasad, S.; O'Dea, J. J.; Osteryoung, J. Mathematical Enhancement of the Performance of Voltammetric Sensors. *Anal. Chim. Acta* **1992**, *264*, 197–204. https://doi.org/10.1016/0003-2670(92)87006-7.

(22) Gavaghan, D. J.; Cooper, J.; Daly, A. C.; Gill, C.; Gillow, K.; Robinson, M.; Simonov, A. N.; Zhang, J.; Bond, A. M. Use of Bayesian Inference for Parameter Recovery in DC and AC Votlammetry. *ChemElectroChem* **2018**, *5* (6), 917–935. https://doi.org/10.1002/celc.201700678.

(23) Li, J.; Kennedy, G. F.; Gundry, L.; Bond, A. M.; Zhang, J. Application of Bayesian Inference in Fourier-Transformed Alternating Current Voltammetry for Electrode Kinetic Mechanism Distinction. *Anal. Chem.* **2019**, *91*, 5303–5309. https://doi.org/10.1021/acs.analchem.9b00129.

(24) Gundry, L.; Guo, S.-X.; Kennedy, G. F.; Keith, J.; Robinson, M.; Gavaghan, D. J.; Bond, A. M.; Zhang, J. Recent Advances for Future Perspectives for Automated Parameterisation, Bayesian Inference and Machine Learning in Voltammetry. *Chem. Commun.* **2021**, *57* (15), 1855–1870. https://doi.org/10.1039/d0cc07549c.

(25) Frkonja-Kuczin, A.; Alicea-Salas, J. Y.; Arroyo-Currás, N.; Boika, A. Hot-SWV: Square Wave Voltammetry with Hot Microelectrodes. *Anal. Chem.* **2020**, *92*, 8852–8858. https://doi.org/10.1021/acs.analchem.0c00427.

(26) Milshtein, J. D.; Barton, J. L.; Carney, T. J.; Kowalski, J. A.; Darling, R. M.; Brushett, F. R. Towards Low Resistance Nonaqueous Redox Flow Batteries. *J. Electrochem. Soc.* **2017**, *164* (12), A2487. https://doi.org/10.1149/2.0741712jes.

(27) Attanayake, N. H.; Kowalski, J. A.; Greco, K. V.; Casselman, M. D.; Milshtein, J. D.; Chapman, S. J.; Brushett, F. R.; Odom, S. A. Tailoring Two-Electron-Donating Phenothiazines To Enable High-Concentration Redox Electrolytes for Use in Nonaqueous Redox Flow Batteries. *Chem. Mater.* **2019**, *31* (12), 4353–4363. https://doi.org/10.1021/acs.chemmater.8b04770.

(28) Lavagnini, I.; Pastore, P.; Magno, F.; Amatore, C. A. Performance of a Numerical Method Based on the Hopscotch Algorithm and on an Oblate Spheroidal Space Coordinate-Expanding Time Grid for Simulation of Voltammetric Curves at an Inlaid Disk Microelectrode. *J. Electroanal. Chem. Interfacial Electrochem.* **1991**, *316* (1), 37–47. https://doi.org/10.1016/0022-0728(91)87034-2.

(29) Birke, R. L. Steady State Concentrations and Currents on an Oblate Spheroid Microelectrode. *J. Electroanal. Chem.* **1989**, *274* (1–2), 297–304. https://doi.org/10.1016/0022-0728(89)87052-4.

(30) Bond, A. M.; Oldham, K. B.; Zoski, C. G. Theory of Electrochemical Processes at an Inlaid Disc Microelectrode under Steady-State Conditions. *J. Electroanal. Chem.* **1988**, *245* (1–2), 71–104. https://doi.org/10.1016/0022-0728(88)80060-3.

(31) Neyhouse, B. J.; Brushett, F. R. From the Synthesis Vial to the Full Cell: Electrochemical Methods for Characterizing Active Materials for Redox Flow Batteries. In *Encyclopedia of Energy Storage*; Cabeza, L. F., Ed.; Elsevier: Oxford, 2022; pp 453–465. https://doi.org/10.1016/B978-0-12-819723-3.00058-5.

(32) Fenton, A. M.; Jha, R. K.; Neyhouse, B. J.; Kaur, A. P.; Dailey, D. A.; Odom, S. A.; Brushett, F. R. On the Challenges of Materials and Electrochemical Characterization of Concentrated Electrolytes for Redox Flow Batteries. *J. Mater. Chem. A* **2022,** *10*, 17988–17999. https://doi.org/10.1039/D2TA00690A.

(33) Goulet, M.-A.; Aziz, M. J. Flow Battery Molecular Reactant Stability Determined by Symmetric Cell Cycling Methods. *J. Electrochem. Soc.* **2018**, *165* (7), A1466–A1477. https://doi.org/10.1149/2.0891807jes].

(34) Nolte, O.; Volodin, I. A.; Stolze, C.; Hager, M. D.; Schubert, U. S. Trust Is Good, Control Is Better: A Review on Monitoring and Characterization Techniques for Flow Battery Electrolytes. *Mater. Horiz.* **2021**, *8* (7), 1866–1925. https://doi.org/10.1039/D0MH01632B.

(35) Niazi, A.; Ghasemi, J.; Zendehdel, M. Simultaneous Voltammetric Determination of Morphine and Noscapine by Adsorptive Differential Pulse Stripping Method and Least-Squares Support Vector Machines. *Talanta* **2007**, *74* (2), 247–254. https://doi.org/10.1016/j.talanta.2007.06.005.

(36) Erickson, J. S.; Shriver-Lake, L. C.; Zabetakis, D.; Stenger, D. A.; Trammell, S. A. A Simple and Inexpensive Electrochemical Assay for the Identification of Nitrogen Containing Explosives in the Field. *Sens. Switz.* **2017**, *17* (8), 1769. https://doi.org/10.3390/s17081769.

(37) Farahani, K. Z.; Benvidi, A.; Rezaeinasab, M.; Abbasi, S.; Abdollahi-Alibeik, M.; Rezaeipoor-Anari, A.; Zarchi, M. A. K.; Abadi, S. S. A. D. M. Potentiality of PARAFAC Approaches for Simultaneous Determination of N-Acetylcysteine and Acetaminophen Based on the Second-Order Data Obtained from Differential Pulse Voltammetry. *Talanta* **2019**, *192*, 439–447. https://doi.org/10.1016/j.talanta.2018.08.092.

(38) Shriver-Lake, L. C.; Myers-Ward, R. L.; Dean, S. N.; Erickson, J. S.; Stenger, D. A.; Trammell, S. A. Multilayer Epitaxial Graphene on Silicon Carbide: A Stable Working Electrode for Seawater Samples Spiked with Environmental Contaminants. *Sens. Switz.* **2020**, *20* (14), 1–9. https://doi.org/10.3390/s20144006.

(39) De Stefano, C.; Ferrigno, L.; Fontanella, F.; Gerevini, L.; Molinara, M. A Novel Evolutionary Approach for IoT-Based Water Contaminant Detection. In *Applications of Evolutionary Computation*; Castillo, P. A., Jiménez Laredo, J. L., Eds.; Lecture Notes in Computer Science; Springer International Publishing: Cham, 2021; pp 781–794. https://doi.org/10.1007/978-3-030-72699-7_49.

(40) Redon, P.; Shahzad, A.; Iqbal, T.; Wijns, W. Development of a New Detection Algorithm to Identify Acute Coronary Syndrome Using Electrochemical Biosensors for Real-World Long-Term Monitoring. *Bioengineering* **2021**, *8* (2), 28. https://doi.org/10.3390/bioengineering8020028.

(41) Bond, A. M.; Zhang, J.; Gundry, L.; Kennedy, G. F. Opportunities and Challenges in Applying Machine Learning to Voltammetric Mechanistic Studies. *Curr. Opin. Electrochem.* **2022**, *34*, 101009. https://doi.org/10.1016/j.coelec.2022.101009.

(42) Gundry, L.; Kennedy, G.; Keith, J.; Robinson, M.; Gavaghan, D.; Bond, A. M.; Zhang, J. A Comparison of Bayesian Inference Strategies for Parameterisation of Large Amplitude AC Voltammetry Derived from Total Current and Fourier Transformed Versions. *ChemElectroChem* **2021**, *8* (12), 2238–2258. https://doi.org/10.1002/celc.202100391.

(43) Adams, A. C.; Jha, S.; Lary, D. J.; Slinker, J. D. Machine Learning for Estimating Electron Transfer Rates From Square Wave Voltammetry. *ChemPlusChem* **2022**, *87* (1), e202100418. https://doi.org/10.1002/cplu.202100418.

(44) Kennedy, G. F.; Zhang, J.; Bond, A. M. Automatically Identifying Electrode Reaction Mechanisms Using Deep Neural Networks. *Anal. Chem.* **2019**, *91* (19), 12220–12227. https://doi.org/10.1021/acs.analchem.9b01891.

(45) Robinson, M.; Simonov, A. N.; Zhang, J.; Bond, A. M.; Gavaghan, D. Separating the Effects of Experimental Noise from Inherent System Variability in Voltammetry: The $[Fe(CN)_6]^{3-/4-}$ Process. *Anal. Chem.* **2019**, *91* (3), 1944–1953. https://doi.org/10.1021/acs.analchem.8b04238.

(46) Ye, J.-J.; Lin, C.-H.; Huang, X.-J. Analyzing the Anodic Stripping Square Wave Voltammetry of Heavy Metal Ions via Machine Learning: Information beyond a Single Voltammetric Peak. *J. Electroanal. Chem.* **2020**, *872*, 113934. https://doi.org/10.1016/j.jelechem.2020.113934.

(47) Movassaghi, C. S.; Perrotta, K. A.; Yang, H.; Iyer, R.; Cheng, X.; Dagher, M.; Fillol, M. A.; Andrews, A. M. Simultaneous Serotonin and Dopamine Monitoring across Timescales by

Rapid Pulse Voltammetry with Partial Least Squares Regression. *Anal. Bioanal. Chem.* **2021**, *413* (27), 6747–6767. https://doi.org/10.1007/s00216-021-03665-1.

(48) Leon-Medina, J. X.; Tibaduiza, D. A.; Burgos, J. C.; Cuenca, M.; Vasquez, D. Classification of As, Pb and Cd Heavy Metal Ions Using Square Wave Voltammetry, Dimensionality Reduction and Machine Learning. *IEEE Access* **2022**, *10*, 7684–7694. https://doi.org/10.1109/ACCESS.2022.3143451.

(49) Dean, S. N.; Shriver-Lake, L. C.; Stenger, D. A.; Erickson, J. S.; Golden, J. P.; Trammell, S. A. Machine Learning Techniques for Chemical Identification Using Cyclic Square Wave Voltammetry. *Sens. Switz.* **2019**, *19* (10), 2392. https://doi.org/10.3390/s19102392.

(50) Kennedy, G. F.; Bond, A. M.; Simonov, A. N. Modelling Ac Voltammetry with MECSim: Facilitating Simulation–Experiment Comparisons. *Curr. Opin. Electrochem.* **2017**, *1* (1), 140–147. https://doi.org/10.1016/j.coelec.2016.12.001.

(51) Northrop, P. W. C.; Cole, J. V. A Pulse Voltammetry Analysis Toolkit for Battery and Fuel Cell Material. *ECS Trans.* **2018**, *85* (5), 23–42. https://doi.org/10.1149/08505.0023ecst.

(52) Gagné, R. R.; Koval, C. A.; Lisensky, G. C. Ferrocene as an Internal Standard for Electrochemical Measurements. *Inorg. Chem.* **1980**, *19*, 2855–2857. https://doi.org/10.1021/ic50211a080.

(53) EC-Lab® Software: Techniques and Applications - Version 10.38, 2014.

(54) Zotti, G.; Schiavon, G.; Zecchin, S.; Favretto, D. Dioxygen-Decomposition of Ferrocenium Molecules in Acetonitrile: The Nature of the Electrode-Fouling Films during Ferrocene Electrochemistry. *J. Electroanal. Chem.* **1998**, *456* (1), 217–221. https://doi.org/10.1016/S0022-0728(98)00279-4.

(55) Molina, A.; Gonzalez, J.; Barnes, E. O.; Compton, R. G. Simple Analytical Equations for the Current-Potential Curves at Microelectrodes: A Universal Approach. *J. Phys. Chem. C* **2014**, *118* (1), 346–356. https://doi.org/10.1021/jp409167m.

(56) Molina, A.; González, J.; Laborda, E.; Compton, R. G. Analytical Solutions for Fast and Straightforward Study of the Effect of the Electrode Geometry in Transient and Steady State Voltammetries: Single- and Multi-Electron Transfers, Coupled Chemical Reactions and Electrode Kinetics. *J. Electroanal. Chem.* **2015**, *756*, 1–21. https://doi.org/10.1016/j.jelechem.2015.07.030.

(57) Alexis M. Fenton, J.; Neyhouse, B. J.; Tenny, K. M.; Chiang, Y.-M.; Brushett, F. R. Extending and Automating Quantitative Microelectrode Voltammetry through an Oblate Spheroidal Coordinate Framework. **2022**. https://doi.org/10.26434/chemrxiv-2022-w5b99.

(58) Bertsekas, D. P.; Tsitsiklis, J. N. *Introduction to Probability*, 2nd ed.; Athena Scientific: Nashua, NH, 2008.

(59) van der Maaten, L.; Hinton, G. Visualizing Data Using t-SNE. *J. Mach. Learn. Res.* **2008**, *9*, 2579–2605.